academicJournals

Vol. 8(19), pp. 754-766, 18 May, 2013
DOI 10.5897/SRE2013.5370
ISSN 1992-2248 © 2013 Academic Journals
http://www.academicjournals.org/SRE

Scientific Research and Essays

Full Length Research Paper

Analytical and computational fluid dynamics (CFD) investigation of the applicability of a ferrofluidic magnetic micropump for fluids with stress-sensitive mircroparticles

M. I. Kilani[1,2]*, M. I. Al-Widyan[1] and A. Al Halhouli[3,4]

[1]College of Engineering, King Faisal University, Al-Ahsa, 31982 Saudi Arabia.
[2]Mechatronics Engineering Department, The University of Jordan, Amman 11942 Jordan.
[3]Mechatronics Engineering Department, German Jordanian University, Mushaqar, Jordan.
[4]Institute of Microtechnology, Technische Universität Braunschweig, Braunschweig, Germany.

Accepted 8 May, 2013

This paper presents analytical and computational fluid dynamics (CFD) investigations of the applicability of a novel ferrofluidic magnetic micropump for fluids with stress-sensitive microparticles. The velocity, pressure, and stress fields in the annular channel of the pump were determined analytically for the case of channels with rectangular cross sections and small aspect ratios ($h/w \rightarrow 0$) under the assumption of laminar incompressible Newtonian flow conditions. CFD simulations were used to produce flow field solutions for the full range of h/w, and to verify the derived analytical expressions. Analytical results show that the velocity and stress fields at a certain radial position in the channel follow that of a Poiseuelle type plug flow scaled by the channel's width ratio over the radial position ratio. A particle damage index (PDI) following the definition of the index of hemolysis (IH) in medical blood pumping was introduced in this work and expressed in terms of pump geometry, plug speed, and working fluid viscosity. Analytical results show that a model ferrofluidic blood pump with a channel width of 100 µm, channel height of 250 µm, and mean radius of 500 µm, can in theory deliver up to 37.5 µl/s of blood without exceeding the threshold design objective PDI of blood pumps.

Key words: Ferrofluidic magnetic micropump, stress-sensitive microparticles, particle damage index, biomedical applications of micropumps.

INTRODUCTION

Recent developments in the design and fabrication of micro-electro-mechanical systems (MEMS) paved the way for the creation of microscale pumps that are capable of pumping fluid samples at the microleter and nanoliter scales (Woias, 2005). The advantages of these pumps include efficient space utilization, lower fabrication costs, lower power budget, portability and precise control on flow rate (Iverson and Garimella, 2008; Ferrari, 2004; Nisar et al., 2008; Bashir, 2004).

Many of the target application of MEMS pumps are concerned with fluids with stress-sensitive microparticles. Typical examples on such applications include chemical analysis (Takashima et al., 2010), biological and chemical sensing (Pilareka et al., 2011; Agudelo et al.,

*Corresponding author. E-mail: mkilani77@yahoo.com. Tel: +962-653 55 000, ext. 23025.

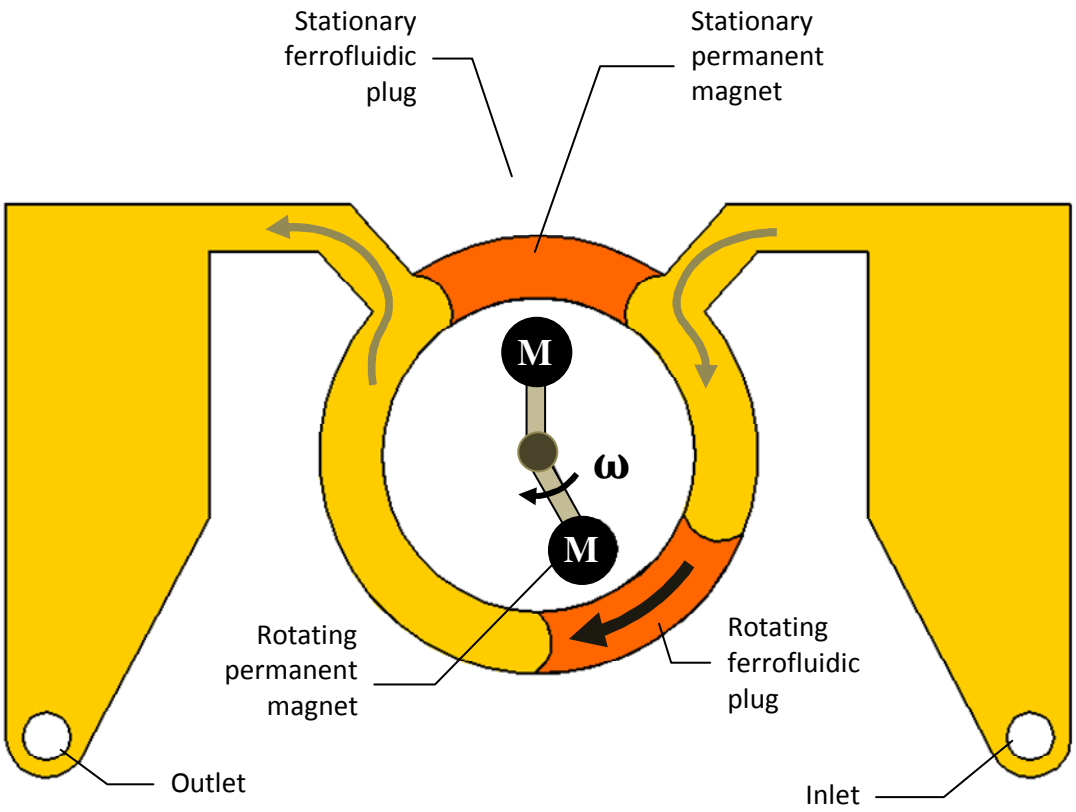

Figure 1. Design and operation of the ferrofluidic magnetic micropump (Hatch, 2001).

2013), drug delivery (Ochoa et al., 2012), molecular separation (Manz et al., 1994) and environmental monitoring (Dutse and Yusof, 2011). The pumped fluid in these applications is characterized by the presence of stress-sensitive particles, which may be damaged due to the abnormal stresses developing in the flow field of the pumping system (Al Halhouli et al., 2012; Mueller et al., 2001; Ruiz et al., 2012; Kilani and Abbadi, 2011). For example, stress-sensitive particles found in such applications include organic molecules, proteins, biopolymers, or living cells and it has been established that flow field stresses on these particles can lead to the alteration of morphology, release of intracellular or extracellular compounds and variation of viability (Bashir, 2004; Stone and Kim, 2001). The successful utilization of a micropump in such applications requires that the maximum shear stresses in the flow field be kept at a level below a certain threshold. In blood pumping applications, for example, the maximum shear stress in the flow field of the pump's channel must be maintained below the lytic shear stress of the red blood cells in order to avoid red blood cell damage, or hemolysis (Bernstein et al., 1967; Leverette et al., 1972).

One micropump design that is potentially promising for application in fluids with stress-sensitive microparticles is the regenerative ferrofluidic magnetic pump (Hatch et al., 2001). The pump is self priming, bubble and particle tolerant, and provides a high compression ratio without compromising power and voltage requirements. An analytical investigation of the shear stresses developing in the flow field of the pump was presented by Kilani et al. (2011). This work investigates the applicability of the pump in applications with stress-sensitive microparticles by estimating the stress distribution in the annular channel of the pump in term of pump geometry, plug speed, and pumped fluid viscosity. A particle damage index (PDI) calculated from the stress distribution and velocity field in the channel is used for estimating the suitability of the pump in those applications.

DESIGN AND OPERATION OF THE FERROLFUIDIC MAGNETIC MICROPUMP

The design and operation of the ferrofluidic magnetic pump is illustrated with reference to Figure 1. The pump utilizes two magnetically-actuated plugs of ferrofluid suspension, which contact but are immiscible with the pumped fluid. Each plug is driven by a permanent magnet which rotates outside the annular channel of the pump in proximity with the plug. In a pumping cycle, one immiscible fluid plug is held stationary in the short section

Table 1. Typical values for the dimensions of a ferrofluidic magnetic micropump (Hatch, 2001).

Parameter	Value
Inner radius (microns)	450
Outer radius (microns)	550
Height (microns)	250
Angular span (rad)	3π/2
Angular speed (rad/s)	50

of the channel between the inlet and outlet, blocking fluid flow through this section, while the other plug is made to rotate along the long section from the inlet to the outlet, pushing the fluid in front of the plug through the outlet port, and simultaneously drawing fluid to the section of the channel behind it through the inlet port. Flow rate can be controlled by adjusting the rotational speed of the moving magnet. Flow can also be reversed by switching the direction of motion of the permanent magnetic plugs. Typical dimensions for the ferrofluidic pump are given in Table 1.

The regenerative ferrofluidic magnetic micropump offers a number of advantages when compared with the popular diaphragm type micropumps (Van Lintel et al., 1988; Schabmueller et al., 2002; Junwu et al., 2005; Lee et al., 2000; Feng and Kim, 2005). Unlike the diaphragm pump where piston displacement is normal to the wafer plane, piston displacement in the ferrofluidic pump occurs in the wafer plane, allowing the pump to have a much larger stroke volume and compression ratio without compromising power and voltage requirements. Additionally, the pump is bubble-tolerant, self priming and valve-less, which makes it potentially suitable for particle-laden fluids characterizing most biomedical applications. The suitability of the pump for biomedical applications, however, is strongly related to the values and distribution of the shear stresses in the pump's flow field. The following sections investigate shear stress distribution in the pump's channel analytically and using CFD.

ANALYTICAL FLOW FIELD MODELING

The flow field in a segment of the pump's channel ahead or behind the moving plug can be modeled as a flow in an annular channel of rectangular cross section as shown in Figure 2, with one wall boundary moving at the speed of the plug v_p and one free boundary maintained at the outlet pressure or inlet pressure p_{out} or p_{in}, for the segment ahead or behind the plug, respectively. For an incompressible Newtonian flow, the continuity and momentum equations are Al Halhouli and Büttgenbach (2010):

$$\nabla.\mathbf{V} = 0 \qquad (1)$$

$$\rho\left[\frac{\partial \mathbf{V}}{\partial t} + \mathbf{V}.(\nabla\mathbf{V})\right] = \mu\nabla^2\mathbf{V} - \Delta p = 0 \qquad (2)$$

where $\mathbf{V}$ is the velocity field and p is the pressure.

Velocity field

This problem is best addressed in cylindrical coordinates assuming a small channel height to width ratio, that is, $h/w \rightarrow 0$, which is the case in the shallow lithographically fabricated microchannels. It is also assumed that the flow is fully developed, laminar and unidirectional in the θ-direction ($v_r = v_z = \partial v_\theta/\partial\theta = 0$) where v_r, v_z and v_θ are the radial, vertical and transverse components of components of $\mathbf{V}$, respectively. The continuity equation (1) is automatically satisfied and the momentum equation (2) in the θ- direction is

$$\mu\left\{\frac{\partial}{\partial r}\left[\frac{1}{r}\frac{\partial}{\partial r}(rv_\theta)\right] + \frac{1}{r^2}\frac{\partial^2 v_\theta}{\partial\theta^2} + \frac{\partial^2 v_\theta}{\partial z^2}\right\} = \frac{1}{r}\frac{\partial p}{\partial\theta} \qquad (3)$$

The inertia and centrifugal forces can be neglected compared to the viscous stresses in the microscale viscosity dominated flow fields. Because of the fully developed flow conditions, the pressure gradient is constant leading to $\partial p/\partial\theta = dp/d\theta = \Delta p/\Delta\theta$, where $\Delta\theta$ is the angular span of the segment of interest in the channel, and Δp is the pressure difference across the segment. Consequently, Equation (3) becomes

$$\mu\frac{\partial^2 v_\theta}{\partial z^2} = \frac{1}{r}\frac{dp}{d\theta} \qquad (4)$$

with the boundary conditions describing stationary lower and upper walls of the channel:

$$v_\theta(r,0) = v_\theta(r,h) = 0 \qquad (5)$$

The velocity field resulting from integrating Equation (4) while applying the boundary conditions in Equation (5) is:

$$v_\theta(r,z) = \frac{h^2}{2\mu}\frac{1}{r}\left[\left(\frac{z}{h}\right)^2 - \frac{z}{h}\right]\frac{dp}{d\theta} \qquad (6)$$

The volumetric flow rate through the channel Q is found to by integrating v_θ over the channel's cross-sectional area as:

$$Q \equiv v_p A = \int_0^h\int_{r_1}^{r_2} v_\theta\, dzdr = \frac{h^3}{12\mu}\ln\left(\frac{r_1}{r_2}\right)\frac{dp}{d\theta} \qquad (7)$$

where $A = h(r_2 - r_1)$ is the cross sectional area of the channel. Equation (7) may be used to relate $dp/d\theta$ to v_p by:

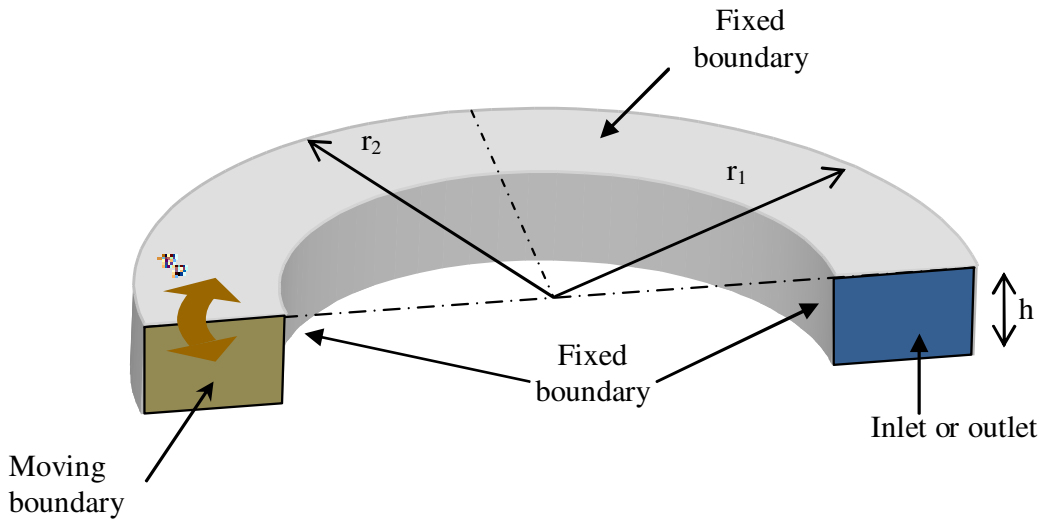

Figure 2. Channel flow model with relevant dimensions.

$$\frac{dp}{d\theta} = -\frac{12\mu(r_2-r_1)}{h^2 ln(r_2/r_1)} v_p \quad (8)$$

An expression for $v_\theta(r,z)$ is obtained using Equations (6) and (8), as:

$$v_\theta(r,z) = 6\frac{r_2-r_1}{ln(r_2/r_1)}\frac{1}{r}\frac{z}{h}\left[1-\frac{z}{h}\right]v_p \quad (9)$$

The expression in Equation (9) can be written in terms of the channel width, $w = r_2 - r_1$, and mean radius $r_m = (r_1 + r_2)/2$ as:

$$v_\theta(r,z) = 6\frac{w}{\ln[(r_m+w/2)/(r_m-w/2)]}\frac{1}{r}\frac{z}{h}\left[1-\frac{z}{h}\right]v_p \quad (10)$$

Pressure field

The pressure field in the segments of the channel ahead and behind the moving plug, p_a and p_b, are readily obtained by integrating Equation (8) between the appropriate boundaries to obtain

$$p_a = p_{out} + 12\frac{\mu w}{h^2 \ln[(r_m+w/2)/(r_m-w/2)]}\theta_{pe} v_p \quad (11)$$

$$p_b = p_{in} - 12\frac{\mu w}{h^2 \ln[(r_m+w/2)/(r_m-w/2)]}\theta_{ip} v_p \quad (12)$$

with θ_{ip} and θ_{pe} standing, respectively, for the angular spans between the channel inlet and the trailing edge of the plug, and between the leading edge of the plug and the channel outlet.

Stress field

The symmetric stress tensor τ_{ij} in cylindrical coordinates is defined by:

$$\tau_{ij} = \begin{bmatrix} 2\mu\frac{\partial v_r}{\partial r} & \mu\left[r\frac{\partial}{\partial r}\left(\frac{v_\theta}{r}\right)+\frac{1}{r}\frac{\partial v_r}{\partial \theta}\right] & \mu\left[\frac{\partial v_z}{\partial r}+\frac{\partial v_z}{\partial z}\right] \\ \tau_{\theta r} & 2\mu\left[\frac{1}{r}\frac{\partial v_\theta}{\partial \theta}+\frac{v_r}{r}\right] & \mu\left[\frac{\partial v_\theta}{\partial z}+\frac{1}{r}\frac{\partial v_z}{\partial \theta}\right] \\ \tau_{zr} & \tau_{z\theta} & 2\mu\frac{\partial v_z}{\partial z} \end{bmatrix} \quad (13)$$

With the assumptions employed, the non-zero components of the stress tensor are:

$$\tau_{r\theta} = \tau_{\theta r} = \frac{6\mu w}{\ln\left[\frac{r_m+w/2}{r_m-w/2}\right]}\frac{1}{r^2}\left[2\left(\frac{z}{h}\right)^2 - 2\left(\frac{z}{h}\right)\right]v_p \quad (14)$$

and

$$\tau_{z\theta} = \tau_{\theta z} = \frac{6\mu w}{\ln[(r_m+w/2)/(r_m-w/2)]}\frac{1}{r^2}\left(\frac{r}{h}\right)\left[2\frac{z}{h}-1\right]v_p \quad (15)$$

A scalar stress value is used based on comparative stress theory of fluids that is analogous to the Mises yield criterion for solid materials, given by Bludszuweit (1995):

$$\tau = \left[\frac{1}{6}\sum(\tau_{ii}-\tau_{jj})^2 + \tau_{ij}\right]^{1/2} \quad (16)$$

For the case considered, the scalar stress reduces to:

$$\tau = \sqrt{\tau_{r\theta}^2 + \tau_{z\theta}^2} \quad (17)$$

Noting that $\tau_{r\theta}^2 \ll \tau_{z\theta}^2$ when $h \ll r$ for $0 \leq z/h \leq 1$, which is the case in the shallow channels of the pump considered, yields

$$\tau \cong \tau_{z\theta} = \pm \frac{6\mu w}{\ln[(r_m + w/2)/(r_m - w/2)]} \frac{1}{rh}\left[2\frac{z}{h} - 1\right] v_p \quad (18)$$

The expression in Equation 18 takes its maximum values at *z* = 0 and *z* = *h,* corresponding the upper and lower walls of the channel

$$\tau_{wall} = \tau_{0,h} = \pm \frac{6\mu w}{\ln[(r_m + w/2)/(r_m - w/2)]} \frac{1}{rh} v_p \quad (19)$$

The average value of τ_{wall} is found with reference to Equation (18) to be

$$\tau_{wall,av} = \pm \frac{1}{(r_2 - r_1)} \int_{r_1}^{r_2} \tau_{wall}\, dr = \pm 6 \frac{\mu v_p}{h} \quad (20)$$

which is exactly equal to the wall shear stress of a Poiseuelle-type plug flow in a rectangular cross-section straight channel with small height-to-width ratio.

PARTICLE DAMAGE INDEX AND CHANNEL DAMAGE INDEX

For the purpose of quantifying the influence of pump flow on stress-sensitive particles, an approach used in macroscale particle pumping devices was employed. The scalar stress *τ* of Equation (18) is used in those applications to calculate a PDI using the following formula (Bludszuweit, 1995).

$$PDI = k \sum_{in}^{out} \tau^m (\Delta t)^n \quad (21)$$

where *k, m,* and *n* are parameters depending on the fluid under investigation, and *t* is the exposure time of a particle to a stress of magnitude *τ* in the flow field. In blood pumping applications, for example, a blood damage index, named the index of hemolysis (IH), is calculated with $\mathrm{k} = 1.8 \times 10^{-6}$, $\mathrm{m} = 1.991$, and $\mathrm{n} = 0.765$ (Giersiepen et al., 1990). The accumulation of stress and exposure time within the pump is integrated along the streamlines to estimate the IH, which is correlated with the relative increase in the concentration of plasma free hemoglobin in the blood due to flow induced stresses along that streamline. A blood pump is clinically acceptable if its average IH is 0.02, while an IH of 0.01 is considered to be a design objective for blood pumps (Nosé, 1998). It is to be noted that the approach employed here does not consider the cumulating of sub-destructive particle damage as presented by Grigioni et al. (2004). To account for this effect, more refined Lagrangian-based descriptors which account for the cumulative sub-destructive damage (Grigioni et al., 2005) may be considered.

To determine the conditions on the exponent n necessary for the PDI in Equation (21) to converge to a non-zero value as $\Delta t \to 0$, we have

$$\lim_{\Delta t \to 0} PDI = \lim_{\Delta t \to 0} (k \sum_{in}^{out} \tau^m (\Delta t)^n) = k(dt)^{n-1} \int_{in}^{out} \tau^m dt \quad (22)$$

which diverges when $n > 1$, converges to zero when $n < 1$, and converges to a non-zero value only when $n = 1$. Under this condition, the expression for PDI in Equation (22) becomes

$$PDI = k \int_{in}^{out} \tau^m dt \quad (23)$$

The Lagrangian expression in Equation (23) is a suitable for representing the stresses experienced by fluid particles using CFD modeling. An Eulerian description of this expression is obtained substituting the kinematic expression $dt = ds/v$ in Equation (23) to obtain

$$PDI = k \int_{in}^{out} \frac{\tau^m}{v} ds \quad (24)$$

where $ds = rd\theta$ is the differential distance traveled by a particle. The path integral in Equation (24) may be evaluated along one streamline from the inlet to the outlet of the channel of the ferrofluidic pump, with $m = 2$ to obtain

$$PDI = k \int_0^t \tau^2 dt = k \int_{\theta_i}^{\theta_o} \frac{\tau^2}{v} r d\theta \quad (25)$$

Equation (25) is evaluated directly since τ, v and r are independent of θ, yielding

$$PDI = 6k \frac{\mu^2 w}{ln\left[\frac{r_m + w/2}{r_m - w/2}\right]} \frac{v_p}{h^2} \Delta\theta \frac{(2z/h - 1)^2}{z/h(1 - z/h)} \quad (26)$$

Equation (26) shows that $PDI \to \infty$ at the upper and lower walls of the channel ($z/h = 0$ and $z/h = 1$). This result is expected since these two boundaries are location of stagnant flow, where particles spend theoretically infinite time. It is also interesting to observe that PDI is independent of r, which is due to the inverse relation between τ and r; a reduced stress as r increases is compensated by an increased lapsed time in the channel.

The area damage index ADI is defined as the average value of PDI over a representative cross-sectional area within the channel, A_n,

$$ADI = \frac{1}{A_n}\int (PDI)dA_n \quad (27)$$

The ADI for a rectangular A_n of width w and height $(z_2 - z_1)$, within the channel of the pump is calculated by substituting $A_n = w(z_2 - z_1)$, $dA_n = wdz$, and the value of PDI_E from Equation (24), to obtain

$$ADI = 6k\frac{\mu^2 w}{\ln\left[\frac{r_m+w/2}{r_m-w/2}\right]}\frac{1}{h(z_2-z_1)}\left[\ln\left(\frac{z_2}{z_1}\right) + \ln\left(\frac{h-z_1}{h-z_2}\right) - 4\left(\frac{z_2}{h} - \frac{z_1}{h}\right)\right]v_p\Delta\theta \quad (28)$$

For the purpose of estimating the damage index of the channel in the ferrofluidic pump, z_1 and z_2 are taken such that A_n is symmetric around the centerline of the horizontal mid-plane of the channel. Substituting $z_1 = h/2 - a/2$, and $z_2 = h/2 + a/2$, where a is the height of A_n, Equation (28) reduces to

$$ADI = 6k\frac{\mu^2 w}{\ln\left[\frac{r_m+w/2}{r_m-w/2}\right]}\frac{1}{ha}\left[\ln\left(\frac{h+a}{h-a}\right) - 2\frac{a}{h}\right]v_p\Delta\theta \quad (29)$$

Noting that $\lim_{a\to 0}\ln\left(\frac{h+a}{h-a}\right) = 2\frac{a}{h}$, ADI vanishes when the width of A_n is equal to w and its height is $a \to 0$ centered around the channel's mid height. This is expected since the mid height of the channel is a location of zero velocity gradient and, therefore, zero shear stresses.

It is also observed that $ADI \to \infty$ if $a \to h$, and a value for a that is a fraction of h must be resorted to in estimating a damage index for an entire channel. A nominal value of $a = 0.99h$ is used in this work to calculate a channel damage of index, designated as CDI, is given by

$$CDI = ADI|_{a=0.99h} = 20.1k\frac{\mu^2 w}{\ln\left[\frac{r_m+w/2}{r_m-w/2}\right]}\frac{1}{h^2}v_p\Delta\theta \quad (30)$$

NON-DIMENSIONAL FORMULATION AND NON-DIMENSIONAL PARAMETERS

Channel width and height ratios

The analytical expressions above may be expressed in terms of dimensionless parameters by defining the non-dimensional radial and vertical positions, respectively, as $r^* \equiv r/r_m$ and $z^* \equiv z/h$. The ratios of the channel width, and channel height to its mean radius, w^* and h^* are defined as

$$w^* \equiv w/r_m = (r_2 - r_1)/r_m = r_2^* - r_1^* \quad (31)$$

$$h^* \equiv h/r_m \quad (32)$$

Since $0 < r_1 < r_2$, it is interesting to observe that $0 < w^* < 2$ for all possible values of r_1 and r_2. The limiting condition $r_1 \to r_2$ leads to $w^* \to 0$, and the flow in the annular channel approaches that of a flow in a straight channel. In contrast, the condition $r_1 \to 0$ results in $w^* \to 2$, and the problem becomes degenerate. The ratio w^* expresses the deviation of the flow in the annular channel from that of a straight channel due to channel curvature.

Equation (28) can be used with the defining relation $r_1 + r_2 \equiv 2r_m$, or $r_2^* + r_1^* = 2$, to determine both r_1^* and r_2^* in terms of w^* using the following formulas

$$r_1^* \equiv 1 - w^*/2 \quad (33)$$

$$r_2^* \equiv 1 + w^*/2 \quad (34)$$

Channel shape factor

The non-dimensional velocity $v_\theta^* \equiv v_\theta/v_p$ may be written in terms of r^* and z^* with reference to Equation (10) as:

$$v_\theta^* = \frac{6w^*}{ln\left(\frac{2+w^*}{2+w^*}\right)}\frac{1}{r^*}\left(z^{*2} - z^*\right) = 6\frac{F_w}{r^*}\left(z^{*2} - z^*\right) \quad (35)$$

where F_w is a channel geometry shape factor that is a function of w^*. A non-dimensional channel shear stress τ^* is defined relative to a reference shear stress $\tau_{ref} = \mu v_p/h$ as

$$\tau^* = \frac{\tau}{\mu v_p/h} = 6\frac{F_w}{r^*}(2z^* - 1) \quad (36)$$

which produces

$$\tau_{wall}^* = \tau_{0,h}^* = \pm 6\frac{F_w}{r^*} \quad (37)$$

and

$$\tau_{wall,av}^* = \pm 6 \quad (38)$$

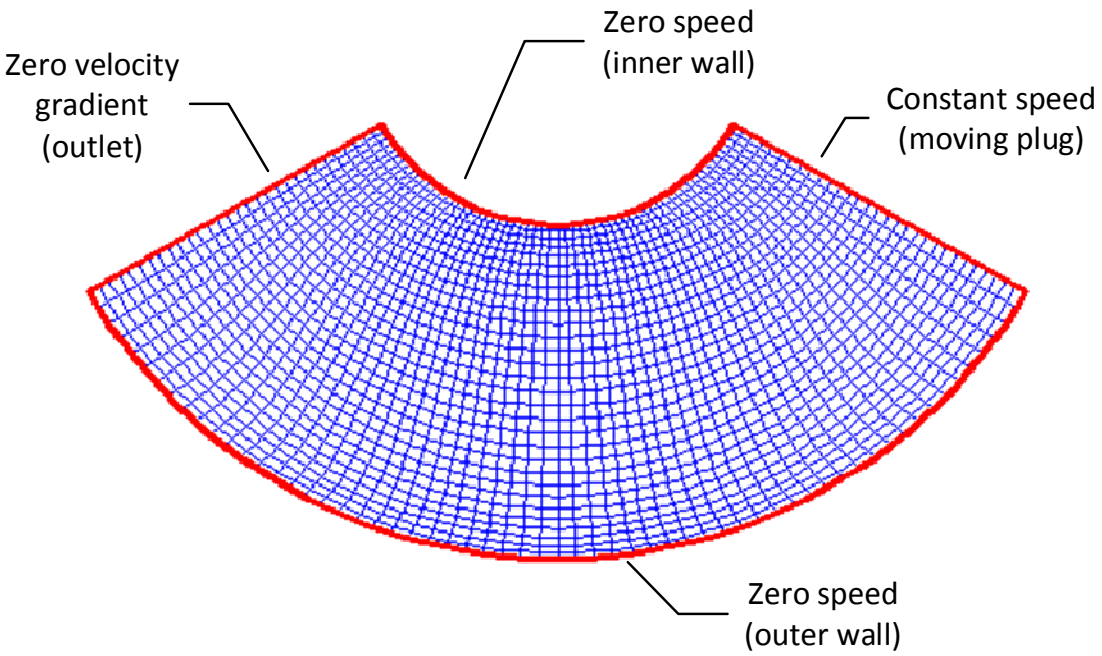

Figure 3. Two dimensional CFD model for the flow field in channel.

Representative area damage factor

Using Eq. (24), a non-dimensional PDI is defined relative to $PDI_{ref} = \frac{k v_p \mu^2 \Delta\theta}{h}$ as

$$PDI^* = PDI/PDI_{ref} = \frac{PDI_E}{v_p \mu^2 \Delta\theta / h} = 6 \frac{F_w}{h^*} \frac{(2z^*-1)^2}{z^*(1-z^*)} \quad (39)$$

The expression for PDI_{ref} above may also serve in defining a non-dimensional area damage index as

$$ADI^* = \frac{ADI}{PDI_{ref}} = 6 \frac{F_w}{h^*} \frac{1}{(z_2^*-z_1^*)} \left[\ln\left(\frac{z_2^*}{z_1^*}\right) + \ln\left(\frac{1-z_1^*}{1-z_2^*}\right) - 4(z_2^* - z_1^*) \right] \quad (40)$$

A representative area centered about the mid height of the channel results in $z_1^* = 0.5 - a^*/2$ and $z_2^* = 0.5 + a^*/2$ with $a^* = a/h$, and the expression in Equation (40) becomes

$$ADI^* = 6 \frac{F_w}{h^*} \frac{1}{a^*} \left[\ln\left(\frac{1+a^*}{1-a^*}\right) - 2a^* \right] = 6 \frac{F_w}{h^*} F_{a^*} \quad (41)$$

where F_{a^*} is a representative area damage factor, which depends on the value of a^* selected for the channel's nominal representative area. If $a^* = 0.99$ as proposed above, the non-dimensional CDI is given by

$$CDI^* = \frac{CDI}{ADI_{ref}} = ADI^*|_{a^*=0.99} = 20.1 \frac{F_w}{h^*} \quad (42)$$

Computational fluid dynamics (CFD) modeling

Both 2-D and 3-D CFD models for the flow field in the ferrofluidic pump were constructed for the purpose of verifying the analytical solution and for the general study of the shear stress distribution in the pump. The Fluent CFD software was used. Fluent provides user interfaces to input problem parameters and to examine the results graphically. It provides mesh flexibility, and support 2D triangular and quadrilateral and 3D tetrahedral, hexahedral, pyramid, wedge, and mixed (hybrid) meshes, making it suitable for solving flow problems with complex geometries.

A 2D Fluent model for the pump prototype was constructed where the cross section of the pump channel assumed to be rectangular with a large height-to-width ratio, which allows approximating the flow in the channel with a 2D model of the flow field at the mid height of the channel as shown in Figure 3. The inner and outer arc boundaries are defined as stationary walls with zero speed, a constant velocity boundary represents the moving face of the piston, and a zero velocity gradient boundary to represent the pump outlet.

A 3-D computational model of the pump's channel was also constructed with different channel heights and was meshed using the CFD pre-processor Gambit. A structured grid with hexahedral elements is defined as the meshing scheme. Pressure inlet, pressure outlet, and zero-velocity with no-slip at the walls were named for the boundary conditions. Fluent uses a finite volume technique to solve for the three dimensional equations of

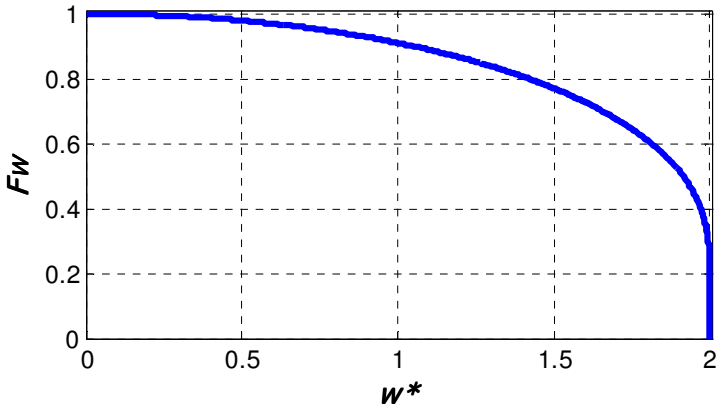

Figure 4. F_w vs. w^* for the full range of w^*.

momentum and continuity. The pressure, momentum, and pressure-velocity coupling were, respectively, achieved through second order, second order upwind, and simple-consistent schemes. The model is defined to be steady state, viscous, laminar, without considering the energy equation, and the solver to be segregated. A viscous fluid with a density of 1260 kg/m^3 and a viscosity of 0.7 kg/m.s was used as the interior fluid. For the convergence criterion, the solver iterated the equations until the scaled residuals were less than 10^{-5} or until it stabilized at a constant value, which is still small enough to ensure convergence. A grid independent solution has been ensured by implementing first different meshes to determine the suitable element size and shape through observing the outlet mass fluxes through the microchannel. The scaled residual for the continuity and momentum equations was also used to judge the convergence of the scaled over the unscaled equations and it is an appropriate indicator for most problems. The solver iterated the equations until the scaled residuals were less than 10^{-5} or until it stabilized at a constant value, which is still small enough to ensure convergence. These issues have been elaborated in Al Halhouli and Büttgenbach (2010).

RESULTS AND DISCUSSION

Velocity distribution

For a channel with a given geometry and plug speed the expression in Equation 26 is recognized as the parabolic profile resulting from a Poiseuelle-type plug flow in straight channel of rectangular cross section, scaled by F_w/r^*. The shape factor F_w is determined by w^* and the plot of F_w vs. w^* in Figure 4 shows that $F_w \to 1$ for $w^* \to 0$, (channel approaching a straight channel) and that $F_w > 0.8$ for $w^* < 1.4$. Since $0 < w^* < 2$, the plot indicates that the flow at $r^* = 1$ approximates that of a Poiseuelle type flow for a wide range of w^* encountered in practical applications.

For a channel with a given geometry, and plug speed Equation (24) indicates that the velocity distribution in the channel follows a Poisuelle profile scaled by F_w/r^*. Consider for example, the velocity distribution for an annular channel with $w^* = 1$, which produces $F_w = 0.91$ The plot in Figure 5 shows this distribution across a section in the channel with $0 \le z^* \le 1$ and $0.5 \le r^* \le 1.5$, which is the range of r^* for this case. The plug speed $v_p^* = 1$ is superimposed on the velocity plot. A straight channel Poiseuelle velocity profile is obtained at $r^* = F_w = 0.9$.

Shear stress

The analytical expression for τ^* given in Equation 35 shows that for a channel with a given F_w, τ^* vanishes at the centerline of the channel ($z^* = 0.5$), and varies directly with z^*, and inversely with r^*. A vanishing τ^*at $z^* = 0.5$ is a result of a zero velocity gradient at that location. The maximum absolute values of τ^* occurs at the upper and lower walls of the channel and are given by Equation 36. According to Equation 37 the average value of the wall stresses $\tau_{wall,av} = \pm 6\tau_{ref} = \pm 6\,\mu v_p/h$ is determined only by μ, v_p and h, and is independent of the other dimensions in the channel. This highlights the important effect of these three parameters on the magnitudes of shear stresses in the channel.

To compare the analytical shear stress results with the CFD predictions, Figure 6 shows a plot of the CFD estimates of τ_w^* vs. r^*/F_w obtained from four different simulations of CFD models with $h/w = 0.1, 0.2, 0.5$ and 1, and $0.2 < r^* < 3$. The analytical estimates of

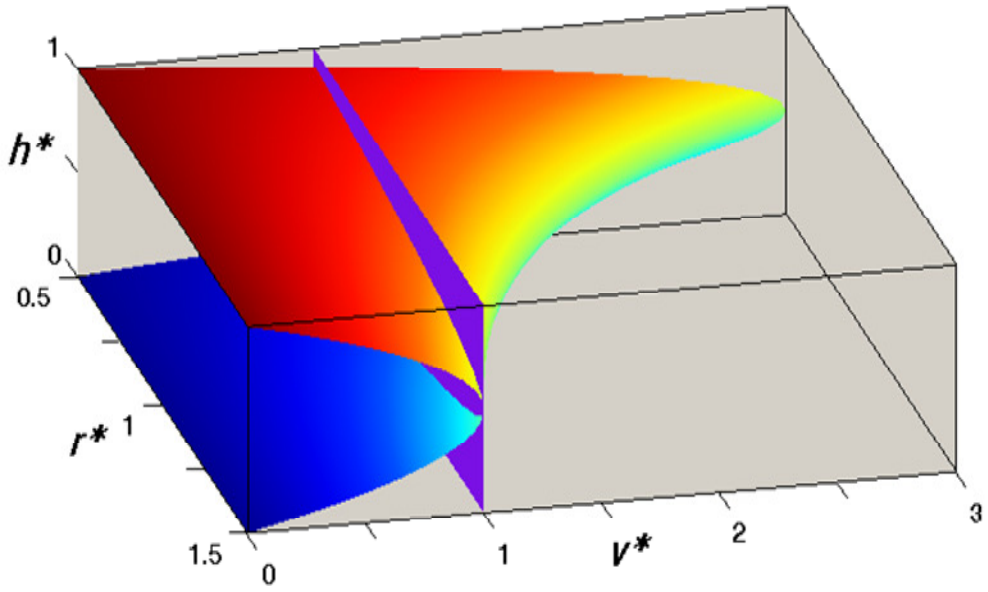

Figure 5. Distribution of v^* across a channel with $0.5 \leq r^* \leq 1.5$.

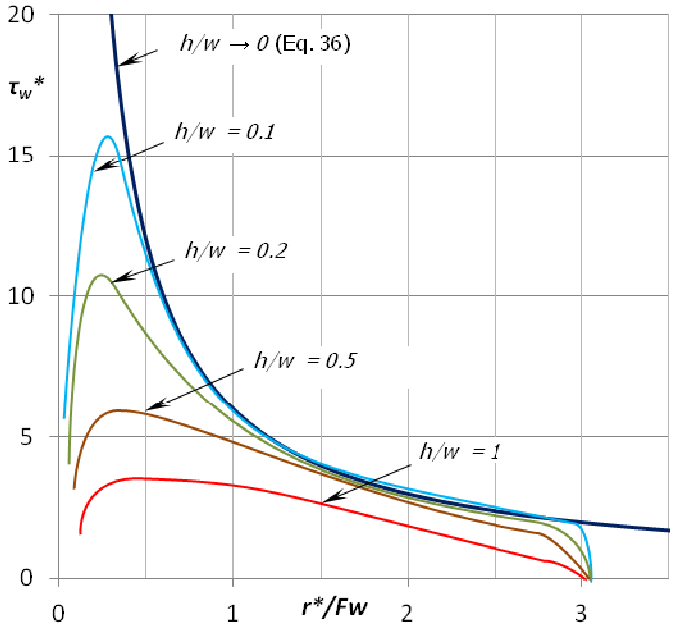

Figure 6. Analytical and CFD estimates of τ^* vs. r^*/F_w.

Equation (36) are sumperimposed on the CFD results of Figure 6 which shows that the analytical and the CFD estimates are almost coincident for the full range of r^* considered up to for $h/w \leq 0.1$, which verifies and supports the analytical expressions derived for $h/w \to 0$. Figure 6 also shows that the CFD estimates fall below the analytical estimates for larger values of h/w. The analytical expressions provide an upper limit on τ_w^* and may be used reliably for a conservative estimate of the scalar wall shear stress across the channel.

Particle damage index and area damage index

The expression for PDI^* in Equation (39) shows that the damage of a certain particles depends on PDI_{ref}, F_w h^* and z^*. The first three of these parameters are determined by the channel geometry, plug speed and fluid viscosity, and are therefore independent the particle's location in the flow field. The influence of z^* on PDI^* is depicted graphically in the plot of Figure 7 for $0 \leq z^* \leq 1$.

The symmetry of the plot in Figure 7 about the mid height of the channel ($z^* = 0.5$) is expected as the problem and its boundary conditions are symmetric about that plane. It is observed that $PDI^* = 0$ at the mid height, which is a consequence of the zero velocity gradient at that plane. It is also worth observing that the PDI^* curve is almost flat around the mid-height of the channel, where the bulk of flow takes place.

Equation (30) may be solved for the height within the channel z^* at which PDI^* takes a certain value giving

$$z^* = \frac{1}{2}\left(1 \mp \sqrt{\frac{PDI^*}{PDI^*+4}}\right) \quad (43)$$

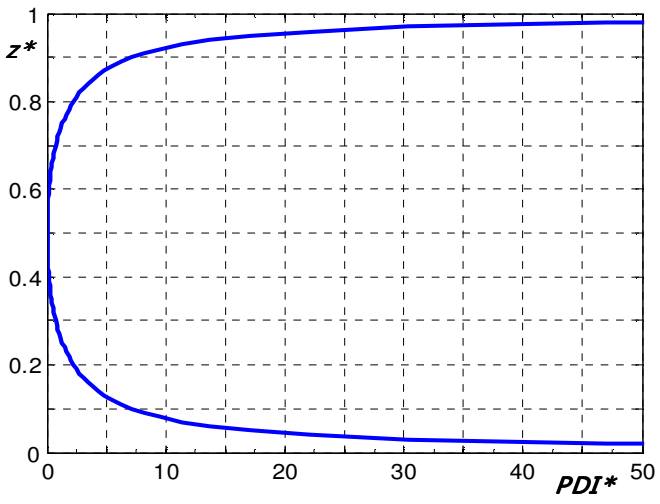

Figure 7. PDI_E^* vs. z^* for $0 \le z^* \le 1$.

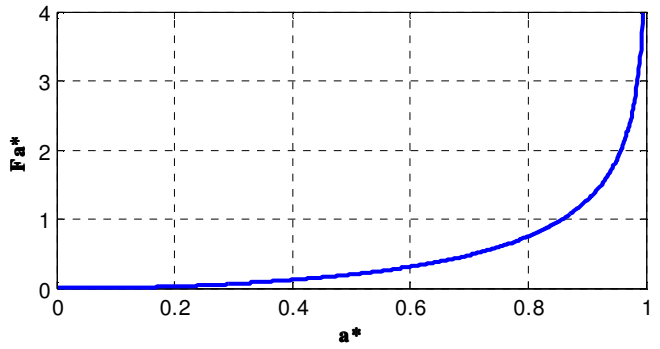

Figure 8. F_a^* versus for a^*.

For $PDI^* = 1$, for example, $z^* = 0.72, 0.28$ indicating that PDI remains below its reference value for $0.28h \le z \le 0.72h$, which represents 44.7% of the channel area.

Equation (30) may also be solved for the percentage of the channel area $A_{\%}$ for which PDI^* remains below a certain value, giving

$$A_{\%} = 100 \times \sqrt{\frac{PDI^*}{PDI^*+4}}\% \quad (44)$$

The expression for ADI^* in Equation (41) shows that the channel damage depends on the parameters ADI_{ref}, F_w h^* and F_{a^*}. The first three of these parameters are determined by the channel geometry, plug speed and fluid viscosity, and are independent of the extent of a^* selected for the nominal representative area in estimating its ADI^*. The influence of a^* on F_{a^*} is depicted graphically in the plot of Figure 8.

As a concrete example, consider the ferrofluidic pump specified in Table 1 operating on human blood ($\mu = 70 \times 10^{-3}$ Pa.s). The value of $CDI = ADI_{99\%}$ calculated from Equation 30 with $k = 1.8 \times 10^{-6}$ and $v_p = \omega r_m = 25 \times 10^{-3}$ m/s is 1.67×10^{-4}, which is well below the target PDI value of 0.01 considered to be a design objective for blood pumps.

Following on this example, consider the problem of estimating the maximum flow rate Q_{max} the abovementioned pump can deliver without reaching the threshold shear stress damage to the blood cells. Using the criterion $\tau_{wall,max} < \tau_{lytic}$, where τ_{lytic} is the lytic shear stress for blood cells, Equation 19 results in

$$\tau_{wall,max} = 1860 v_{p,max} = 1860 \frac{Q_{max}}{hw} < \tau_{lytic} \quad (45)$$

where $v_{p,max}$ is the plug speed producing Q_{max}. Substituting the lytic shear stress of blood for long exposure time $\tau_{lytic} = 0.25$ kPa Sutera and Mehrjardi (1975), in Equation 45 produces $Q_{max} = 3.36$ µl/s, which occurs at $v_p = 0.134$ m/s. This Q_{max} estimate ignored the stress magnitudes away from the upper and lower inner corners, which are well below $\tau_{wall,max}$, and through which a significantly larger portion of the flow takes place. Additionally, the angular span of the pump $\Delta\theta$ was not considered in the calculation, which is not realistic, since a longer channel must results in a longer exposure time and, consequently, less admissible pump flow.

A more realistic Q_{max} estimate obtained using the criterion $ADI_{99\%} < PDI_{lytic}$ can be calculated from Equation 30 with $k = 1.8 \times 10^{-6}$ and $\Delta\theta = 3\pi/2$ results in

$$CDI = ADI|_{a=0.99h} = 0.007 v_{p,max} = 0.007 \frac{Q_{max}}{hw} < PDI_{lytic} \quad (46)$$

Using $PDI_{lytic} = 0.01$Pa^{2}s results in $Q_{max} = 37.5$ µl/s at a theoretical $v_p = 1.5$ m/s.

Scale shear stress distribution for channels with non-zero aspect ratios

The distribution of the scalar shear stress in the channel's mid plane is shown in Figure 9, while Figure 10 shows the distribution in a representative section across a vertical section in the channel. The shear stress is almost zero in the majority of the flow field inside the channel

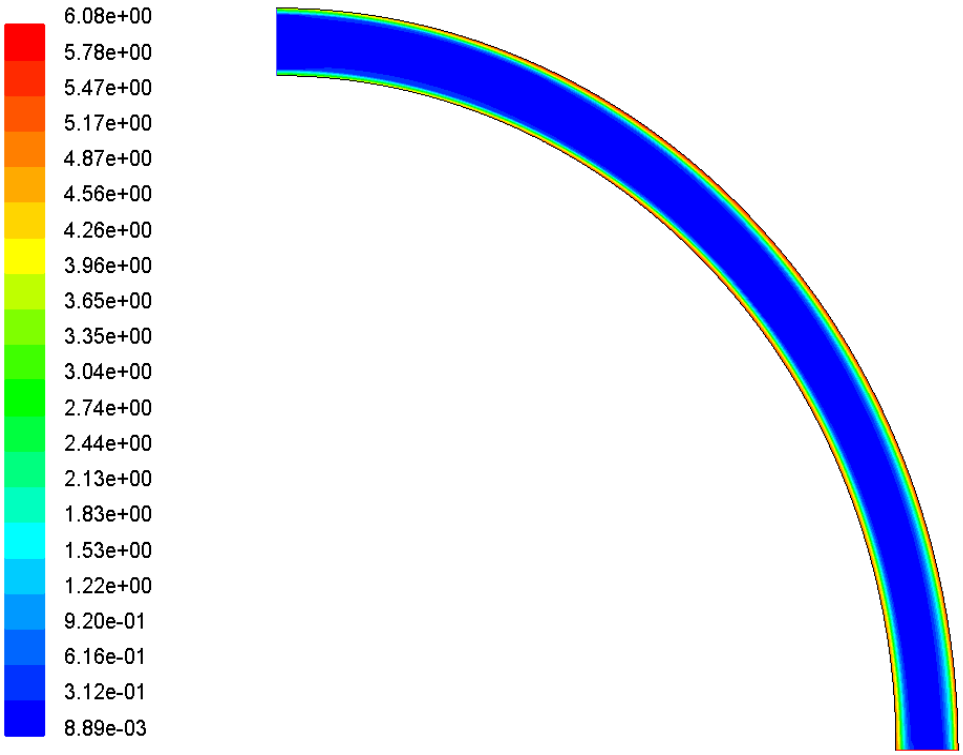

Figure 9. Stress distribution in the channel's mid plane.

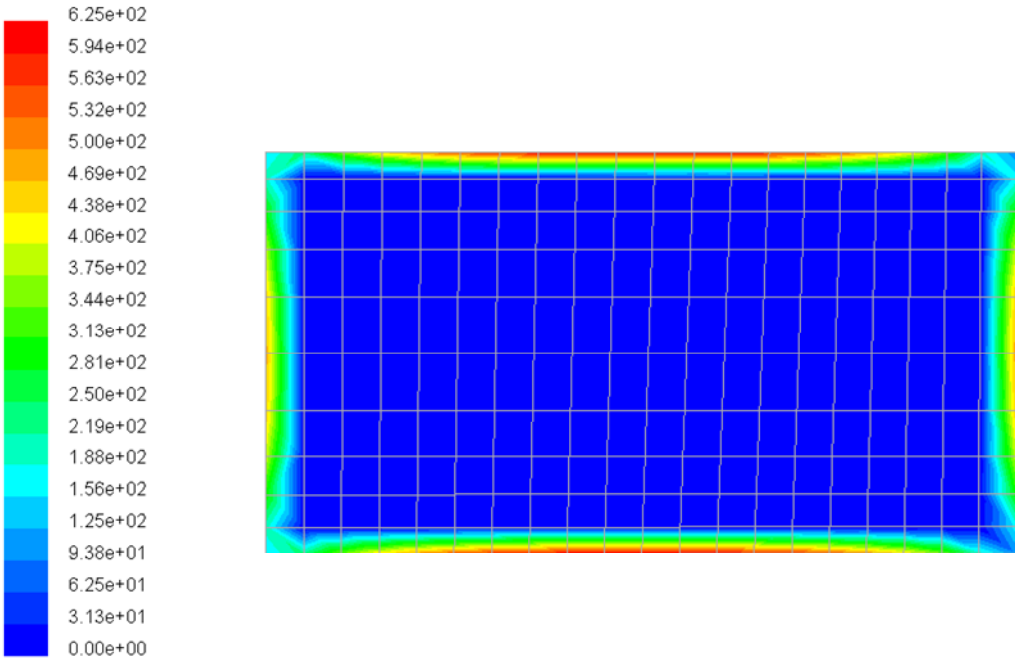

Figure 10. Stress distribution in a vertical plane across the channel.

and becomes significant only in the thin strips near the walls of the channel. Away from the wall, the shear stress ranges from 1 to 5% of its wall values. Since the major portion of the flow takes place away from the wall, this

distribution is very compatible with the requirements imposed by fluids with stress sensitive microparticles, as it indicates that most of the pumped particles will be exposed to relatively low stress values for a short period of time.

Conclusions

The paper presented analytical and CFD investigations of the applicability of a ferrofluidic magnetic micropump for fluids with stress-sensitive microparticles. The velocity, pressure and stress fields in the annular channel of the pump were determined analytically for laminar incompressible Newtonian flow for pump channels with rectangular cross sections and small aspect ratios (*h/w*→ 0) by solving the Navier-Stokes equations in polar coordinates. Analytical and simulation results indicate that the velocity and stress profiles in the channel follow that of a Poisuelle type plug flow in a rectangular cross-section straight channel scaled by F_w/r^*. The analytical predictions of the velocity and shear distribution were found to be in very good agreement with CFD results for $h/w \to 0$. For larger values of h/w, the CFD predictions were found to be lower than the analytical predications irrespective of the value of h/w, indicating that the analytical estimates provide an upper limit on the shear stress and may be used reliably for a conservative estimate of the shear stress distribution.

CFD simulations have also demonstrated the for channel with finite aspect ratios, the shear stress takes a significant magnitude only in narrow strips near the walls of the channel, and is very small in the rest of the channel, where the major portion of the flow takes place. This was also supported by the shape of the PDI^* curve, which is almost flat around the mid-height of the channel, where the bulk of flow takes place. This is a favorable feature for particle-laden applications as it indicates that most of the pumped particles will be exposed to relatively low stress values for a short period of time.

The PDI introduced in this work follows the definition of the IH used in clinical blood pumping, and depends on pumped particles exposure time to shear stresses in the pump flow field. The PDI was related to pump geometry, plug speed, and working fluid viscosity. Analytical results show that a model ferrofluidic blood pump with $w = 100$ µm, $h = 250$ µm, and $r_m = 500$ µm, can in theory deliver up to 37.5 µl/s of blood before exceeding the threshold design objective PDI for blood pumps. Considering the favorable characteristics reported in "design and operation of the ferrolfuidic magnetic micropump" part of this work of the investigated micropump for fluids with stress-sensitive microparticles, the abovementioned findings support the suitability of the pump for such fluids not only for the microscale, but also for macroscale appplications.

ACKNOWLEDGMENTS

The authors wish to acknowledge the Deanship of Scientific Research at King Faisal University, Al-Ahsa, Saudi Arabia for supporting and providing the fund for this work.

Nomenclature: A, Channel cross sectional area, (M^2); ADI, representative area damage index; *A*, symmetric representative area height; CDI, channel damage index; F, shape factor; *H*, channel height, (m); *K*, damage index contant; v, pressure (Pa); PDI, particle damage index; Q, volumetric flow rate (m^3/s); *R,* radial coordinate, radius (m); *T,* time; v, speed (m/s); V, velocity (m/s); *W,* channel width (m); Z, vertical coordinate.

Greek Symbols: µ, Dynamic viscosity (Pa.s); ρ, Mass density, (kg/m^3); τ, Shear stress (Pa); *θ,* Tranverse coordinate, radians.

Subscripts: *1,* inner; *2,* outer; *Av,* average; *M,* Mean; *N,* nominal; *i,j,* indices; *in,* inlet; *out,* outlet; *p,* plug; *R,* radial direction; *Ref,* reference; *W,* width; *Wall,* wall; *Z,* vertical direction; *θ,* transverse direction.

Superscript: *, dimensionless; *m,n,* exponent.

Notations: *Δ,* Difference; *D,* derivative; ∂, partial derivative; Lim, limit.

REFERENCES

Agudelo CG, Nezhad AS, Ghanbari M, Naghavi M, Packirisamy M, Geitmann A (2013). TipChip: a modular, MEMS-based platform for experimentation and phenotyping of tip-growing cells. Plant J. 73(6):1057-1068.

Al Halhouli AT, Büttgenbach S (2010). Liquid Flow in Curved Microchannels. Int. J. Theor. Appl. Multiscale Mech. 1(3):253-265.

Al Halhouli AT, Kilani MI, Waldschik A, Phataralaoha A, Büttgenbach S (2012). Development and testing of a synchronous micropump based on electroplated coils and microfabricated polymer magnets. J. Micromech. Microeng. 22(6):1-8.

Bashir R (2004). BioMEMS: state-of-the-art in detection, opportunities and prospects, Adv. Drug Deliv. Rev. 56(11):1565-1586

Bernstein EF, Blackshear PL, Keller KH (1967). Factors influencing erythrocyte destruction in artificial organs. Am. J. Surg. 114(1):126–138.

Bludszuweit C (1995) Three-Dimensional Numerical Prediction of Stress Loading of Blood Particles in a Centrifugal Pump. Artif. Organs. 19(7):583-589.

Dutse S, Yusof NA (2011). Microfluidics-Based Lab-on-Chip Systems in DNA-Based Biosensing: An Overview. Sensors 11(6):5754-68.

Feng GH, Kim ES (2005). Piezoelectrically actuated dome-shaped diaphragm micropump. J. Microelectromech. Syst. 14(2):192-199.

Ferrari M (Ed.) (2004). Biomedical Nanotechnology. Kluwer Acad. Pub.

Giersiepen M, Wurzinger LJ, Optiz R, Reul H (1990). Estimation of Shear Stress Related Blood Damage in Heart Valve Prostheses: In Vitro Comparison of 25 Aortic Valves. Artif. Organs. 13(5):300-306.

Grigioni M, Daniele C, Morbiducci, U, D'Avenio G, Di Benedetto G,

Barbaro V (2004). The power-law mathematical model for blood damage prediction: Analytical developments and physical inconsistencies. Artif. Organs. 28(5):467-475.

Grigioni M, Morbiducci U, D'Avenio G, Di Benedetto G, Del Gaudio C (2005). A novel formulation for blood trauma prediction by a modified power-law mathematical model. Biomech. Model. Mechanobiol. 4(4):249-260.
Hatch A, Kamholz AE, Holman G, Yager P, Böhringer KF (2001). A Ferroflu-idic Magnetic Micropump. J. Microelectromech. Syst. 10(2):215-221.
Iverson BD, Garimella SV (2008). Recent advances in microscale pumping technologies: a review and evaluation. Microfluid Nanofluid. 5(2):145-174.
Junwu K, Zhigang Y, Taijiang P, Guangming C, Boda W (2005). Design and test of a high performance piezoelectric micropump for drug delivery. Sens. Actuators A: Phys. 121(1):156-161.
Kilani MI, Abbadi A (2011). Pump for fluids with stress-sensitive microparticles. UK Patent GB 2477276 A.
Kilani MI, Al-Halhouli A, Büttgenbach S (2011). Shear Stress Analysis in a Ferrofluidic Magnetic Micropump. Nanoscale Microscale Thermophys. Eng. 15(1):1- 15.
Lee SW, Sim WY, Yang SS (2000). Fabrication and *in vitro* test of a microsyringe. Sens. Actuators A: Phys. 83(13):17-23.
Leverette LB, Hellums JD, Alfrey CP, Lynch EC (1972). Red blood cell damage by shear stress. Biophys. J. 12(3):257-273
Manz A, Effenhauser CS, Burggraf N, Harrison DJ, Seiler K, Flurri K (1994). Electroosmotic pumping and electrophoretic separations for miniaturized chemical analysis systems. J. Microelectromech. Syst. 4(4):257-265.
Mueller XM, Boone Y, Augstburger M, Horisberger J, von Segesser LK (2001). Bi-ventricular axial micropump: Impact on blood cell integrity. Swiss Surg. 7(5):213-217.
Nisar A, Afzulpurkar N, Mahaisavariya B, Tuantranont A (2008). MEMS-based micropumps in drug delivery and biomedical applications. Sens. Actuator B-Chem. 130(2):917-942.
Nosé Y (1998). "Design and development strategy for the rotary blood pump." Artif. Organs. 22(4): 438-446.
Ochoa M, Mousoulis C, Ziaie B (2012). Polymeric microdevices for transdermal and subcutaneous drug delivery. Adv. Drug Deliv. Rev. 64(14):1603-1616.
Pilareka M, Neubauerb P, Marxc U (2011). Biological cardio-micro-pumps for micro-bioreactors and analytical micro-systems. Sens. Actuator B-Chem. 156(2):517-526.
Ruiz J, Closas A, Fernandez A, De Pouplana L (2012). Impulsion core for a fluid micropump. Patent No. EP2511529 A1
Schabmueller C, Koch M, Mokhtari ME, Evans A, Brunnschweiler A, Sehr S (2002). Self-aligning gas/liquid micropump. J. Micromech. Microeng. 12(4):420-424.
Stone HA, Kim S (2001). Microfluidics: Basic Issues, Applications, and Challenges. AIChE J. 47(6):1250-1254.
Sutera, SP, Mehrjardi MH (1975). Deformation and fragmentation of human RBC in turbulent shear flow. Biophys. J. 15(1):1-10.
Takashima A, Kojima K, Suzuki H (2010). Autonomous microfluidic control by chemically actuated micropumps and its application to chemical analyses. Anal. Chem. 82(16):6870-6876.
Van Lintel H, van De Pol F, Bouwstra S (1988). A piezoelectric micropump based on micromachining of silicon. Sens. Actuators. A 15 (2):153-167.
Woias P (2005). Micropumps - Past, Progress and Future Prospects. Sens. Actuator B-Chem. 105(1):28-38.